Raman Scattering from Electronic Excitations in n-Type Silicon Carbide[†]

Priscilla J. Colwell[*] and Miles V. Klein

Department of Physics and Materials Research Laboratory,
University of Illinois, Urbana, Illinois 61801

We have performed Raman measurements at 8 K on the $6H$ polytype of SiC nominally doped with 4×10^{18} and 6×10^{19} nitrogen donors per cm^3. The 4×10^{18} samples showed electronic transitions of E_2 symmetry at 13.0, 60.3, and 62.6 meV that we interpret as $1s(A_1)$ to $1s(E)$ valley-orbit transitions at the three inequivalent donor sites having symmetries that are, respectively, hexagonal, cubic, and cubic. To check the assignment of the electronic transitions to the inequivalent sites we studied the Raman spectrum of the $15R$ polytype of SiC doped with nitrogen. This polytype has five inequivalent sites: two hexagonal and three cubic. We observed two transitions at roughly 7.7 and 11.6 meV, which we assign to the hexagonal sites, and two levels at 50.6 and 54.9 meV and possibly a level at 46.0 meV, which we assign to the cubic sites. These large site-dependent differences in energy within the donor ground state point to a breakdown of effective-mass theory. The E_2 symmetry of these transitions in the $6H$ polytype was used to show that the conduction-band minima must lie along the line ML at the edge of the Brillouin zone. An interference was observed between the 13-meV electronic transition and an E_2 phonon of the pure crystal ($6H$) at 18.6 meV. We have proposed a phenomenological theory and obtained the electron-phonon coupling constant from a fit to theory. The 6×10^{19} sample revealed a Raman continuum with E_2 symmetry extending to about 65 meV that interfered strongly with the 18.5-meV phonon and also with a 33.1-meV E_2 phonon. The E_2 symmetry and the interference effect suggest that the continuum retains some properties of localized levels even at concentrations greater than 2×10^{19}, where the metallic transition occurs. This sample also exhibited LO-phonon-plasmon coupling. The high-frequency mode (L_+) was observed and was highly asymmetric with $\omega_p \tau \sim \frac{1}{3}$. These parameters were found by assuming the line shape to be proportional to Imϵ^{-1}, where ϵ is the total dielectric constant. Due to the large damping the low-frequency mode (L_-) was broadened and very small compared to the high-frequency mode. Finally an E_2 vibrational mode in the gap region of the SiC phonon spectrum was observed at 78.8 and 79.6 meV for nitrogen concentrations of 4×10^{18} and 6×10^{19}, respectively, in the $6H$ polytype and at 78.6 meV in the $15R$ polytype.

I. INTRODUCTION

Nitrogen-doped silicon carbide is a wide-band-gap multivalley n-type semiconductor that grows in many polytypes. The $6H$ polytype, used in this investigation, has an hexagonal structure with the same space group (C_{6v}^4) as wurtzite. Until this investigation, no Raman measurements had been performed on any polytype of nitrogen-doped silicon carbide. Moreover, there have been relatively few spectroscopic investigations concerning the nature of the donor levels. Estimates of donor ionization energies have been obtained from previous work, but there is disagreement among the results. This paper reports on Raman measurements on degenerate (6×10^{19} cm^3) and nondegenerate (4×10^{18}/ cm^3) nitrogen-doped $6H$ silicon carbide and a few measurements on nondegenerate nitrogen-doped $15R$ silicon carbide.

Among the 12 atoms in the unit cell of $6H$ SiC there are three crystallographically inequivalent nitrogen-donor sites. Two of the sites have a cubic, zinc-blende arrangement of first and second neighbors, and the other site has a hexagonal or wurtzite arrangement. We review here those previous results that are relevant to our work.

A. Optical Properties of $6H$ SiC: N

Optical and thermal-luminescence measurements have given evidence that nitrogen occupies the three crystallographically inequivalent sites on the carbon sublattice. Choyke and Patrick have observed emission from recombination of excitons at sites they assigned to neutral or singly ionized nitrogen.[1,2] Since the exciton is bound to an impurity atom it may recombine without emitting a phonon. Three such phonon-free lines appeared in the spectrum assigned to neutral nitrogen.[1] Two of the lines had essentially the same intensity and were very close in energy, being 31 and 32.5 meV below the exciton energy gap; the third line was less intense, and was 16 meV below the exciton energy gap. The more intense a phonon-free line is, the more localized the donor to which the exciton is bound. Patrick suggested that the less-intense third line was due to nitrogen on the hexagonal sites, and the other two lines to nitrogen on the cubic sites.[3] The phonon-assisted emission showed three series of lines; these series were attributed to nitrogen on the three inequivalent sites.[1,2] From these spectra they estimated a lower limit for each of the three nitrogen ionization energies: 0.17,

0.20, and 0.23 eV.[2] Gorban *et al.* measured the thermoluminescence of 6H SiC:N and obtained the following ionization energies: 0.18, 0.21, and 0.24 eV.[4]

B. ESR and NMR Properties of 6H SiC:N

Nitrogen acts as a paramagnetic impurity in the diamagnetic SiC host lattice and results in spin-resonance absorption. Woodbury and Ludwig performed electron-spin resonance (ESR) and electron-nuclear double resonance (ENDOR) on a 6H SiC sample having a nitrogen content of $3 \times 10^{16}/cm^3$.[5] The experimental value of the nuclear g factor determined from the ENDOR results was in agreement with the known nuclear g factor for N^{14}. Since the nuclear spin of N^{14} is 1, the ESR spectrum should exhibit three, equally intense, hyperfine lines. They observed two overlapping sets of three lines which were interpreted as being due to an equal distribution of nitrogen among the three inequivalent sites, with two of the sites giving essentially the same spin-resonance behavior. They showed that the hyperfine interaction was isotropic. This indicated that the ground-state wave function of the donor electron was predominantly s like. van Wieringen also observed that the donor electron was s like.[6]

van Wieringen measured the ESR spectrum at 77 K of samples whose nitrogen content ranged from $\sim 10^{17}/cm^3$ to $1.1 \times 10^{19}/cm^3$; these concentrations (n_D) were determined by Lely and Kröger[7] from Hall-effect measurements. At low concentrations the three hyperfine lines were observed; these experiments did not permit the resolution of the two overlapping series of three lines seen by Woodbury and Ludwig. As the nitrogen concentration increased, the central line increased in height and width relative to the other two lines until at $1.1 \times 10^{19}/cm^3$ only the central peak remained. This gave evidence of some delocalization of the donor electrons, since at higher concentrations a donor electron may wander over two or more nitrogen nuclei due to wave-function overlap between donors. In this case, the hyperfine structure is averaged out. Iglitsyn *et al.* have also observed these effects.[8] van Wieringen found that for a concentration of paramagnetic centers of up to $3 \times 10^{18}/cm^3$ there was agreement between the paramagnetic concentration and the Hall-effect concentration. For the sample with the Hall-effect concentration of $1.1 \times 10^{19}/cm^3$, the paramagnetic concentration was $4 \times 10^{18}/cm^3$.

Hardeman performed ESR and ENDOR on a series of nitrogen-doped SiC crystals.[9] The ESR spectrum of a sample having a nitrogen content of $\sim 10^{19}/cm^3$ showed a single line at 77 K, but at 1.2 K hyperfine structure existed. From the ENDOR results the Bohr radius of the donor electron was found to be

5.0 Å.

In order to study the delocalization of donor electrons due to donor-electron wave-function overlap, Alexander performed nuclear magnetic resonance (NMR) at 1.2, 4.2, and 77 K on SiC samples having nitrogen content $1.9 \times 10^{19}/cm^3$, $4.2 \times 10^{19}/cm^3$, and $6.0 \times 10^{19}/cm^3$.[10] This range of concentration was chosen since electron-transport measurements indicated that a "metallic transition" to a delocalized electronic system occurred at donor concentrations $\sim 2 \times 10^{19}/cm^3$. The NMR results showed that the Si^{29} spin-lattice relaxation time was independent of temperature at liquid-helium temperatures. There was no detectable Knight shift for both Si^{29} and C^{13}. The NMR linewidths showed a definite temperature dependence, with the lines narrowing as the temperature increased. The results were interpreted as being characteristic of localized centers; by "localized," it was meant that electrons were bound to donor sites or complexes of donor sites. The narrowing of the NMR linewidths as the temperature increased gave evidence that some of the localized electrons were thermally excited so that they were delocalized at higher temperatures. From the NMR linewidths the concentration of the localized paramagnetic electrons was found to be $4 \times 10^{18}/cm^3$, in agreement with van Wieringen's result. The final interpretation of the NMR results was that the "metallic transition" may indeed occur at $n_D \sim 2 \times 10^{19}/cm^3$, but that there remains a small concentration of localized electrons. These results are unique to 6H SiC:N; no such results have been reported for heavily doped Si or Ge.[11]

C. Electron-Transport Properties of 6H SiC:N

Lely and Kröger measured the Hall coefficient and resistivity of nitrogen-doped SiC for concentrations from $10^{17}/cm^3$ to $5 \times 10^{19}/cm^3$ over a temperature range 90–1000 K.[7] They found that the "metallic transition" occurred for a donor concentration of $\sim 2 \times 10^{19}/cm^3$. Violina *et al.* performed the same measurements for a concentration range of 1×10^{17} to $2 \times 10^{19}/cm^3$; again, for the $2 \times 10^{19}/cm^3$ SiC:N sample, metallic behavior was found.[12] Both of these reports showed that the mobility decreased as the nitrogen concentration increased; the mobilities ranged from 360 cm^2/V sec for the lowest concentration[12] to about 10 cm^2/V sec for the highest concentration.[7]

The high-temperature Hall data have been analyzed to find values for the donor binding energy E_D that are consistently near 0.085 eV.[7,8,13,14] Thus, there appears to be a significant discrepancy between the ionization energy obtained from Hall-effect measurements (0.085 eV) and from luminescence measurements (0.17–0.23 eV).

Our Raman results have extended our knowledge of the properties of nitrogen in SiC. For the non-

degenerate samples we have observed valley-orbit electronic Raman transitions $[1s(A_1) \rightarrow 1s(E)]$ for nitrogen on the three inequivalent sites in the $6H$ polytype and for nitrogen on the five inequivalent sites in the $15R$ polytype. These transitions occurred in widely separated energy regions, and are interpreted as due to donors on the hexagonal sites for the transitions occurring at smaller energies and for donors on the cubic sites for the transitions occurring at larger energies. The symmetry of these valley-orbit transitions is used to show that the conduction-band minima in $6H$ SiC lie along the line ML in the Brillouin zone. The nondegenerate samples also showed a Raman interference effect between the excited state of one of the electronic transitions and a host-crystal E_2 phonon of approximately zero wave vector. A phenomenological model is proposed that assumes a mixing between the donor electron and phonon states, and a fit to the interference line shape was obtained. A vibrational impurity mode was observed in both the nondegenerate and degenerate samples.

The spectrum for the degenerate sample showed a continuum that had a pronounced interference effect with several host-crystal E_2 phonons, had the same symmetry as the valley-orbit transitions, and extended to about the same energy as the higher-energy valley-orbit transitions. These results suggest that the donor-electron wave functions retained some nonmetallic characteristics even though the samples were degenerate, and thus add to the ESR and NMR results which picture the donor electrons as being not completely metallic. At the same time, this sample showed a shifted, asymmetric, LO phonon that is attributed to a coupled plasmon–LO-phonon mode, whose asymmetry is due in part to a very short electron-collision lifetime. A preliminary version of this work has been given elsewhere.[15]

We present the remainder of this paper in the following sections: Sec. II gives background information on the band structure and the first-order Raman-active phonons of the host crystal; Sec. III describes the samples, the experimental procedure, and the selection rules; Sec. IV discusses the theory for Raman scattering from donors, and discusses coupled LO-phonon–plasmon modes; Sec. V gives the results; Sec. VI discusses the results for the nondegenerate samples; Sec. VII discusses the results for the degenerate samples; and Sec. VIII summarizes the paper.

II. CONDUCTION-BAND MINIMA, CRYSTAL STRUCTURE, AND PHONONS OF THE HOST CRYSTAL

The $6H$ polytype of silicon carbide has an indirect gap[16] with an exciton energy gap of 3.024 eV.[1] The valence-band maximum is at the center of the Brillouin zone, and a spin-orbit-split band lies 4.8

meV below this maximum.[1] The crystal-field-split valence band is believed to be more than 30 meV below the highest valence bands.[1]

There has been disagreement over the location of the conduction-band minima in the Brillouin zone. Ellis and Moss[17] measured the Hall coefficient parallel and perpendicular to the $\vec{c}$ axis, found it to be isotropic, and concluded that the minima are ellipsoids of revolution located on the $\vec{c}$ axis. With this location of the minima they found the values of the effective-mass tensor from their Faraday rotation and absorption measurements: $m_\perp^* = (0.25 \pm 0.02)m$ and $m_\parallel^* = (1.5 \pm 0.2)m$.[17] Choyke and Patrick concluded from the phonons observed in exciton recombination radiation that there are 12 minima located off the $\vec{c}$ axis, and that they are located in the mirror plane (ΓML) near the boundary of the Jones zone.[1,18,19]

Junginger and van Haeringen used the empirical-pseudopotential method to calculate the electronic band structure of the $6H$ polytype.[20] They calculated the energy levels at the Brillouin-zone points Γ, K, H, A, M, and L, and found that the conduction-band minima occurred at the M point. From their graph it is seen that the ΓL gap appears to be about 0.15 eV larger than the ΓM gap; this is within the 0.2-eV uncertainty in the computed levels. Herman *et al.* used an interpolation procedure based on their orthogonalized-plane-wave calculation for the cubic and wurtzite polytypes of SiC to show that the minima in $6H$ SiC would lie along the line ML in the Brillouin zone.[21] If the minima lie at the M point or the L point there would be three minima, and if they lie between M and L there would be six conduction-band minima.

Crystal Structure and Phonons

The $6H$ polytype belongs to the C_{6v}^4 ($P6_3mc$) space group and has 12 atoms per unit cell. This means that there are 33 $q = 0$ optic phonons of which 27 are active in first-order Raman scattering. The Raman-active modes have A_1, E_1, and E_2 symmetry. The E_1 and E_2 modes are doubly degenerate. There is also a silent B_1 mode for this space group.

In order to keep track of all the $q = 0$ phonons it is convenient to introduce a large zone for $6H$,[1] extending to $6\pi/c$, where c is the axial dimension of the unit cell. The maximum wave vector of the Brillouin zone is π/c. The Brillouin zone is thus obtained from the large zone by folding the large zone five times. Defining a reduced wave vector $\chi = q/q_{max}$ for the large zone, it is seen that the points $\chi = 0$, 0.33, 0.67, and 1.0 are $q = 0$ wave vectors in the Brillouin zone. Figure 1(a) shows the large zone and the Brillouin zone for $6H$ SiC in the direction of the $\vec{c}$ axis.

Figure 1(b) shows the large-zone location and symmetry of the $q = 0$ phonons observed by Feldman
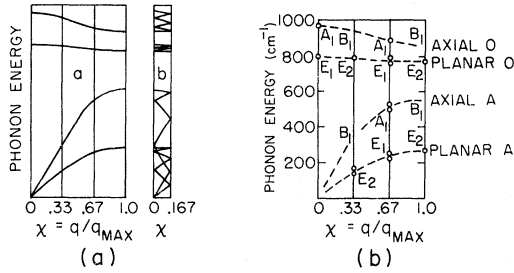
FIG. 1. (a) The axial dispersion curves (schematic) for phonons in $6H$ SiC (from Ref. 22) for the large zone (left-hand side) and for the Brillouin zone (right-hand side). The abscissa is $\chi = q/q_{max}$, where $q_{max} = 6\pi/c$. (b) The observed $q = 0$ Raman-active phonons plotted on the large-zone dispersion curves. The phonon energy unit is cm^{-1}. The symbol O stands for optic and A for acoustic.

et al.[22] In the figure O stands for optic and A for acoustic. Note that at $\chi = 0.33$ and 0.67, doublets occur. They are due to the details of the stacking sequence. If the force constants between planes depended only on the distance between planes then the dynamical matrix for the $6H$ structure would have the same translational symmetry as that for the zinc-blende structure (along the [111] direction), and the phonon spectrum would be smooth inside the large zone, since the large zone is the Brillouin zone for zinc blende in the [111] direction. In fact, the force constants also depend on the types of layers, hexagonal or cubic, in the $6H$ structure. This dependence results in the occurrence of doublets.[23]

We present the phonon energies determined by Feldman *et al.* in Table I. The upper number in the table is in units of meV and the lower in units of cm^{-1}; the letter F means forbidden and N. O. means not observed; the labels A(xial) O(ptic), etc., apply only for $\chi \neq 0$. Moreover, for the crystal orientations on which we have performed backscattering measurements there are no mixed symmetries, so we have omitted the mixed-symmetry mode ($\chi = 0$ phonons) energies from the table. It should be noted that Feldman *et al.* used a right-angle scattering geometry for their measurements; their data were taken at room temperature.

The rhombohedral $15R$ polytype has ten atoms per unit cell, and space group R_{3m}. The Raman-active (first-order) A_1 and E phonons have been studied by Feldman *et al.*[24] The $15R$ polytype has five inequivalent sites: two hexagonal and three cubic.

The site symmetry for a donor in both $6H$ and $15R$ SiC is C_{3v}, since the atoms in all SiC polytypes have tetrahedral coordination. The Raman-active modes for the C_{3v} representation are A_1 and E. An impurity mode having E symmetry should appear in both E_1 and E_2 Raman polarization geometries.

III. EXPERIMENTAL

A. Samples

Three different concentrations of nitrogen in $6H$ SiC were used here. All the samples were single crystals, in the form of parallel platelets with hexagonal edges; the thin direction was along the $\vec{c}$ axis.

The purest sample investigated was obtained from Dr. W. J. Choyke of the Westinghouse Electric Corp., Pittsburgh, Pa., and was numbered D-94-RA-9. According to Choyke the sample had a nitrogen content of roughly 10^{17}/cm^3 as determined from a brief look at the photoluminescence at liquid-nitrogen temperature. The sample was transparent and colorless.

Several samples having a nitrogen content of 4×10^{18}/cm^3 (see below) were transparent and had a medium-green color; these samples (batch S-4) were obtained from Dr. W. D. Compton, who obtained them in turn from Dr. P. T. B. Shaffer of the Carborundum Co., Niagara Falls, N. Y. All spectra where the direction of the laser beam was parallel to the $\vec{c}$ axis were taken on a sample for which Schein had measured a room-temperature resistivity (perpendicular to the $\vec{c}$ axis) of about $0.25 \, \Omega \, \text{cm}$.[25] Another sample was mounted so that the normal to one of the hexagonal sides, i.e., the $\vec{a}$ axis, was parallel to the direction of the laser beam; this crystal had a room-temperature resistivity of $0.14 \, \Omega \, \text{cm}$.

The most-heavily doped sample had a nominal nitrogen content of 6×10^{19}/cm^3. It was opaque and

TABLE I. The zero-wave-vector phonon energies of $6H$ SiC.[a] The labels for the phonons are the same as those of Fig. 1. The upper number for the phonon energy is in units of meV, and the lower in units of cm^{-1}. B_1 modes are forbidden (F), and two expected components of doublets were not observed (N. O.).

$\chi = 0$	Branch	$\chi = 0.33$	$\chi = 0.67$	$\chi = 1$
E_1(LO) 120.3 / 970	Axial O	B_1(F)	A_1 110.2 / 889	B_1(F)
A_1(LO) 119.5 / 964		B_1(F)	A_1 N.O.	
E_1(TO) 98.8 / 797	Planar O	E_2 97.7 / 788	E_1 96.3 / 777	E_2 95.0 / 766
A_1(TO) 97.7 / 788		E_2(N.O.)	E_1 95.3 / 769	
	Axial A	B_1(F)	A_1 63.0 / 508	B_1(F)
		B_1(F)	A_1 62.5 / 504	
	Planar A	E_2 18.5 / 149	E_1 29.9 / 241	E_2 32.5 / 262
		E_2 18.0 / 145	E_1 29.3 / 236	

[a]Reference 22.

colored blue black before polishing and black after polishing; this sample and many others from the same batch (634) were also obtained from Shaffer. Schein and Compton measured several samples from batch 634 and found that the carriers were degenerate.[26]

Violina et al. have measured the resistivity, Hall constant, and mobility for several concentrations of SiC : N; the values $N_D - N_A$, N_A, and E_D were obtained from the Hall-constant curves, where N_D is the number of donors, N_A the number of acceptors, and E_D the donor ionization energy.[12] For a room-temperature resistivity of 0.2 Ω cm they found $N_D - N_A = 4.5 \times 10^{17}/cm^3$, $N_A = 1.1 \times 10^{17}/cm^3$, and $E_D = 63$ meV. Lely and Kröger, however, have measured the same properties for many concentrations and found for $E_D = 64$ meV that $N_D - N_A$ was $3.1 \times 10^{18}/cm^3$ and N_A was $1.5 \times 10^{18}/cm^3$, thus differing by an order of magnitude from Violina et al.[7]

Lely and Kröger determined $N_D - N_A$ for many concentrations and also found N_D from a chemical analysis. They plotted the concentrations determined from both of these measurements as a function of the square root of the N_2 overpressure used for crystal growth. They found that they could draw a straight line through the data; an overpressure of 1 atm corresponded to a nitrogen content of $6 \times 10^{19}/cm^3$.

Slack and Scace checked the extrapolation of this graph by a vacuum-fusion analysis of a crystal grown under 35 atm of N_2 and found reasonable agreement.[27] Thus the graph of Lely and Kröger appears to be a good way of finding the nitrogen content to within, say, ±25%.

The Lely and Kröger value of $3.1 \times 10^{18}/cm^3$ quoted above falls below the line on their graph; the line gives $4 \times 10^{18}/cm^3$. Thus, for our samples with resistivity 0.25 and 0.14 Ω cm we estimate the nitrogen content as $4 \times 10^{18}/cm^3$.

It should be noted that the samples used in Alexander's nuclear-magnetic-resonance study of heavily doped (greater that $1.9 \times 10^{19}/cm^3$) SiC : N were also obtained from Shaffer, and, moreover, both Shaffer and Alexander used Lely and Kröger's graph for obtaining the nitrogen content.[10] Also in these heavily doped samples both Alexander and Shaffer found by chemical analysis that compensation of the donors was not important, and this result presumably applies to our $6 \times 10^{19}/cm^3$ sample.

A 15R polytype sample of SiC : N was also investigated. The crystal was transparent and yellow green in color. One edge, however, showed the medium-green color of the $4 \times 10^{18}/cm^3$ 6H SiC : N samples, and thus we assume the nitrogen content of this sample was also roughly $4 \times 10^{18}/cm^3$.

All sample surfaces (except the $\vec{a}$ surface) were polished with $\frac{1}{4}$-μm diamond polish. The samples were mounted on copper disks with G. E. 7031 var-

nish; the disks had a hole in the center so that the transmitted laser light could escape through the back of the cryostat.

B. Experimental Equipment

An argon-ion laser, which produced over 1 W at 5145 Å, was used in these experiments. The double monochrometer was the Spex model 1400 with Jobin-Yvon gratings (blaze-5000 Å, 1200 lines/mm), which showed no grating ghosts in the wavelength ranges covered here. The light from the monochrometer exit slit was focussed onto an ITT FW-130 photomultiplier (PM) tube, having S-20 response, and the signal from the PM tube was detected either by current detection or by photon counting.

The cryostat used for low-temperature work was an Andonian 3-liter variable-temperature Dewar in which the sample was cooled by helium gas obtained by expansion of the liquid helium through a throttle valve, a capillary, and a diffuser. We found that having the sample directly in cold gas was important for heavily doped samples where absorption of the laser light caused internal heating. Use of a heater on the sample block and a heater on the diffuser allowed achievement of a wide temperature range. Temperatures were measured with an annealed gold + 0.07-at.% iron vs copper thermocouple[28] attached to the sample block. We estimate an accuracy of ± 2 K in temperature measurement and stability.

All data were taken using a back-scattering optical geometry which has been described in a previous publication.[29]

C. Raman Selection Rules

As mentioned above, the 6H polytype has three Raman-active $q = 0$ phonon symmetries, A_1, E_1, and E_2. A_1 and E_1 phonons are also infrared active, while E_2 is only Raman active. The Raman tensors for phonons having these symmetries have been given by Poulet[30] and Loudon,[31] and their components are experimentally determined by the polarization directions of the laser and Raman light. The notation $\vec{k}_L(\vec{\lambda}_L, \vec{\lambda}_R)\vec{k}_R$ is used to denote the laser- and Raman-light propagation directions, $\vec{k}_L$ and $\vec{k}_R$, and the laser- and Raman-light polarization directions, $\vec{\lambda}_L$ and $\vec{\lambda}_R$.

Table II lists the phonon symmetries which can be seen under the experimental conditions used here. In the table, $\overline{Z}$ is along the negative $\vec{c}$ axis.

IV. THEORY

In this section we present the theory for electronic Raman scattering from donor electrons and the theory for Raman scattering from coupled plasmon—LO-phonon modes.

TABLE II. The geometries used in this investigation and allowed phonon symmetries. $\bar{Z}$ is along the negative c axis.

$\bar{Z}(XX)Z$	$\bar{Z}(XY)Z$	$\bar{Z}(YY)Z$	$\bar{Z}(YX)Z$
A_1(LO), E_2	E_2	A_1(LO), E_2	E_2
$\bar{X}(YY)X$	$\bar{X}(YZ)X$	$\bar{X}(ZZ)X$	$\bar{X}(ZY)X$
A_1(TO), E_2	E_1(TO)	A_1(TO)	E_1(TO)

A. Raman Scattering from Donor Levels

The first observation of the electronic Raman effect in semiconductors was by Henry et al.[32] There has been much recent activity in this area.[33]

Shallow donors in semiconductors that have their conduction-band minimum at zero wave vector have a hydrogenic set of energy levels that lie just below the conduction band. These levels are described by the effective-mass approximation.[34] For a multivalley semiconductor, where the conduction-band minima are not at zero wave vector, the $1s$ hydrogenic donor level splits due to valley-orbit coupling among states associated with the various equivalent conduction-band minima[34]; transitions among these levels are called valley-orbit transitions. Most of the Raman transitions previously observed for donors have been valley-orbit transitions. Wright and Mooradian have given a theoretical expression of the cross section for valley-orbit Raman transitions.[35] They used the effective-mass approximation and considered virtual interband transitions to two bands, one lying above the conduction band and the other below it. In this section we consider a two-band model (conduction and valence bands) and obtain a result similar to theirs. We present this to show that the valley-orbit transition is the strongest electronic Raman transition, and to show that the selection rules for Raman scattering from valley-orbit levels depend on the orientation of the inverse-effective-mass tensor in the Brillouin zone.

For a multivalley semiconductor whose conduction-band minima lie at the points $\vec{k}_j$ in the Brillouin zone, the effective-mass-donor-electron wave function is a linear combination of the wave functions for each minimum and is given by[34]

$$\psi(\vec{r}) = \sum_{j=1}^{N} \alpha_j^{(v)} F_j(\vec{r}) u_j(\vec{r}) e^{i\vec{k}_j \cdot \vec{r}} . \tag{1}$$

In the expression, N is the number of equivalent minima, and $\alpha_j^{(v)}$ are numerical coefficients for group representation v of the impurity Hamiltonian, $u_j(\vec{r})$ is the periodic part of the Bloch function at the jth minimum and ϵ_0 is the static dielectric con-envelope function. For the conduction-band minimum at $\vec{k} = 0$, the envelope function satisfies the

equation

$$\left(-\frac{\hbar^2}{2m^*} \nabla^2 + \frac{e^2}{\epsilon_0 r} \right) F(\vec{r}) = E F(\vec{r}) , \tag{2}$$

where m^* is the effective mass at the conduction-band minimum, and ϵ_0 is the static dielectric constant. The energy eigenvalues are given by

$$E_n = -E_B^*/n^2 , \quad E_B^* = \frac{m^*(e^2/\epsilon_0)^2}{(2\hbar^2)} , \tag{3}$$

where E_B^* is the binding energy. The envelope functions are given by hydrogenic wave functions whose Bohr radius is

$$a^* = \hbar^2 \epsilon_0 /(m^* e^2) . \tag{4}$$

For anisotropic effective-mass and dielectric-constant tensors which possess cylindrical symmetry, the energy eigenvalues and wave functions are more complicated.[36,37] We will use the results given above, however, in order to estimate the strengths of various electronic Raman processes.

The Hamiltonian describing the interaction of radiation with electrons in matter is given by

$$H = \sum_{i=1}^{N} \frac{1}{2m} \left(\vec{P}_i - \frac{e_i}{c} \vec{A}(\vec{r}_i, t) \right)^2 + V(\vec{r}_1, \vec{r}_2, \ldots, \vec{r}_N)$$

$$= H_0 + H_1 + H_2 , \tag{5}$$

where, for the Coulomb gauge,

$$H_0 = \sum_{i=1}^{N} \frac{P_i^2}{2m} + V(\vec{r}_1, \vec{r}_2, \ldots, \vec{r}_N) , \tag{6}$$

$$H_1 = -\sum_{i=1}^{N} \frac{e_i}{mc} [\vec{P}_i \cdot \vec{A}(\vec{r}_i, t)] , \tag{7}$$

$$H_2 = \sum_{i=1}^{N} \frac{e_i^2}{2mc^2} A^2(\vec{r}_i, t) . \tag{8}$$

Raman scattering from donor states requires the use of H_1 in second-order time-dependent perturbation theory. The H_2 term will not be important since the energy of the radiation field is much smaller than the energy of an atomiclike system. For a single donor there is only one term in the sum over i in H_1. The differential Stokes-Raman scattering cross section is given by

$$\frac{d^2\sigma}{d\Omega_R d\omega_R} = \left(\frac{e}{mc} \right)^4 \frac{\omega_R}{\omega_L} \sum_n |\sum_m|^2 \delta(\omega - \omega_{n0}) , \tag{9}$$

where $\hbar\omega_L (\hbar\omega_R)$ is the energy of the laser (Raman) photon, ω_{n0} is the excitation frequency $\omega_n - \omega_0 = (E_n - E_0)/\hbar$, and $\omega = \omega_L - \omega_R$. The $\sum_m$ stands for

$$\sum_m \equiv \sum_m \left(\frac{\langle n | \vec{P} \cdot \vec{\lambda}_L | m \rangle \langle m | \vec{P} \cdot \vec{\lambda}_R^* | 0 \rangle}{E_0 - E_m - \hbar\omega_R} \right.$$

$$\left. + \frac{\langle n | \vec{P} \cdot \vec{\lambda}_R^* | m \rangle \langle m | \vec{P} \cdot \vec{\lambda}_L | 0 \rangle}{E_0 - E_m + \hbar\omega_L} \right) , \tag{10}$$

where $\vec{\lambda}_L(\vec{\lambda}_R^*)$ are the laser (Raman) photon polarizations, and $|m\rangle$ is an intermediate state of the scattering system.

To evaluate $\sum_m$ we assume an explicit, simple model for the energy bands in the semiconductor. We use a two-band model for a solid with indirect gaps at $\vec{k}_j$ of amount E_G. Within the two-band model there are three types of Raman transitions that can occur among the donor-energy levels.

(i) An electron initially in the ground state of the $1s$ manifold undergoes a virtual transition to the valence band via the first momentum operator. The second momentum operator takes the electron back to another level in the $1s$ manifold. The result of this process is that one observes a Raman transition among valley-orbit levels.

(ii) An electron starting from the ground state of the $1s$ manifold again makes a virtual transition to the valence band, but the second momentum operator takes it to a higher hydrogenic level, say, $2s$. One thus observes a $1s$ to $2s$ transition of the donor electron.

(iii) An electron starting from the ground state undergoes a virtual transition to a higher, odd-parity, hydrogenic level, and then goes to an even parity level either in the $1s$ manifold or not in it. We could observe a valley-orbit transition or a $1s$ to $2s$ transition, for example.

To evaluate processes (i) and (ii) we have only one intermediate state, the valence band, so we may use closure to obtain

$$\sum_m = \sum_{\alpha,\beta=1}^{3} (\lambda_L)_\alpha (\lambda_R^*)_\alpha \left(\frac{1}{E_G - \hbar\omega_R} \langle n|P_\alpha P_\beta|0\rangle \right.$$
$$\left. + \frac{1}{E_G + \hbar\omega_L} \langle n|P_\beta P_\alpha|0\rangle \right), \quad (11)$$

where we have labelled the Cartesian components of $\vec{\lambda}_L(\vec{\lambda}_R^*)$ by $\alpha(\beta)$.

We write the donor-electron wave functions ψ_0 and ψ_n as

$$\psi_0(\vec{r}) = \sum_{j=1}^{N} \alpha_j^{(v)} F_{j0}(\vec{r}) u_j(\vec{r}) e^{i\vec{k}_j \cdot \vec{r}}, \quad (12)$$

$$\psi_n(\vec{r}) = \sum_{j'=1}^{N} \alpha_{j'}^{(w)} F_{j'n}(\vec{r}) u_{j'}(\vec{r}) e^{i\vec{k}_{j'} \cdot \vec{r}}. \quad (13)$$

The matrix element $\langle n|P_\alpha P_\beta|0\rangle$ thus becomes

$$\langle n|P_\alpha P_\beta|0\rangle = \sum_{j,j'} \alpha_{j'}^{(w)*}\alpha_j^{(v)} \int d\vec{r}\, F_{j'n}^*(\vec{r}) u_{j'}^*(\vec{r})$$
$$\times e^{-i\vec{k}_{j'}\cdot\vec{r}} P_\alpha P_\beta F_{j0}(\vec{r}) u_j(\vec{r}) e^{i\vec{k}_j\cdot\vec{r}}. \quad (14)$$

The coordinate $\vec{r}$ can be written as the sum of a vector $\vec{R}$ giving the position of a unit cell in the crystal and a vector $\vec{\tau}$ giving positions within the unit cell; that is, $\vec{r} = \vec{R} + \vec{\tau}$. The origin of $\vec{r}$ is the donor nucleus. $F(\vec{r})$ is essentially constant over a unit cell and is thus characterized by $\vec{R}$; we

write, therefore, $F(\vec{R})$. The integral $\int d\vec{r}$ is written

$$\int d\vec{r} = \sum_R \Omega \int_{\text{cell}} \frac{d\vec{\tau}}{\Omega} \rightarrow \int d\vec{R} \int_{\text{cell}} \frac{d\vec{\tau}}{\Omega}. \quad (15)$$

We thus obtain

$$\langle n|P_\alpha P_\beta|0\rangle = \sum_{jj'} \alpha_{j'}^{(w)*}\alpha_j^{(v)}\{ \int d\vec{R}\, F_{j'n}^*(\vec{R}) F_{j0}(\vec{R})$$
$$\times \int d\vec{\tau}\, \Omega^{-1} e^{-i(\vec{k}_{j'}-\vec{k}_j)\cdot\vec{\tau}}$$
$$\times u_{j'}^*(\vec{\tau})(P_\alpha + \hbar k_{j\alpha})(P_\beta + \hbar k_{j\beta}) u_j(\vec{\tau})$$
$$+ \int d\vec{R}\, F_{j'n}^*(\vec{R})[P_\alpha P_\beta F_{0j}(\vec{R})]$$
$$\times \int d\vec{\tau}\, \Omega^{-1} e^{-i(\vec{k}_{j'}-\vec{k}_j)\cdot\vec{\tau}} u_{j'}^*(\vec{\tau}) u_j(\vec{\tau})\}. \quad (16)$$

In the expression we have operated with $P_\alpha P_\beta$ on the envelope function and periodic function and have used parentheses to signify the extent of the remaining operations. We have also omitted two cross terms where one momentum operator acts on $F(\vec{R})$ and the other on $u_j(\vec{\tau})$, since such terms will not contribute to the Raman processes that we wish to calculate.

By expanding $u_{j'}^*(\vec{\tau})(P_\alpha + \hbar k_{j\alpha})(P_\beta + \hbar k_{j\beta}) u_j(\vec{\tau})$ and $u_{j'}^*(\vec{\tau}) u_j(\vec{\tau})$ as a Fourier series in reciprocal-lattice vectors, one can show that j must equal j' and thus expression (16) becomes

$$\langle n|P_\alpha P_\beta|0\rangle = \sum_j \alpha_j^{(w)*}\alpha_j^{(v)}[\int d\vec{R}\, F_{jn}^*(\vec{R}) F_{j0}(\vec{R})$$
$$\times \int d\vec{\tau}\, \Omega^{-1} u_j^*(\vec{\tau})$$
$$\times (P_\alpha + \hbar k_{j\alpha})(P_\beta + \hbar k_{j\beta}) u_j(\vec{\tau})$$
$$+ \int d\vec{R}\, F_{jn}^*(\vec{R}) P_\alpha P_\beta F_{j0}(\vec{R})]. \quad (17)$$

Within this two-band model we can express $\langle u_j|(P_\alpha + \hbar k_{j\alpha})(P_\beta + \hbar k_{j\beta})|u_j\rangle$ in terms of the effective-mass tensor by using $\vec{k}\cdot\vec{P}$ perturbation theory. We obtain

$$\langle u_j|(P + \hbar k_j)_\alpha (P + \hbar k_j)_\beta|u_j\rangle = \tfrac{1}{2} mE_G \left[\left(\frac{m}{m^*}\right)_{\alpha\beta} - \delta_{\alpha\beta} \right]_j. \quad (18)$$

The following relation holds:

$$\langle u_j|(P + \hbar k_j)_\alpha (P + \hbar k_j)_\beta|u_j\rangle$$
$$= \langle u_j|(P + \hbar k_j)_\beta (P + \hbar k_j)_\alpha|u_j\rangle. \quad (19)$$

Thus for process (1) with $|n\rangle = |0\rangle = |1s\rangle$ we obtain

$$\sum_m = \frac{mE_G^2}{E_G^2 - (\hbar\omega_L)^2} \sum_{\alpha,\beta=1}^{3} (\lambda_L)_\alpha (\lambda_R^*)_\beta$$
$$\times \sum_{j=1}^{N} \alpha_j^{(w)*}\alpha_j^{(v)} \left[\left(\frac{m}{m^*}\right)_{\alpha\beta} - \delta_{\alpha\beta} \right]_j$$
$$+ \frac{4}{3} \frac{m^* E_B^* E_G}{E_G^2 - (\hbar\omega_L)^2} \sum_{\alpha,\beta=1}^{3} (\lambda_L)_\alpha (\lambda_R^*)_\beta \sum_{j=1}^{N} \alpha_j^{(w)*}\alpha_j^{(v)}. \quad (20)$$

In this expression the second term is nonzero only if the initial and final state have the same group representation. In addition, this second term has the ratio $\frac{4}{3}(m^*/m)(E_B^*/E_G)$ to the first term (where we took the quantities in the sum over j as unity). This ratio is small (estimates will be given in Sec. V); we will drop the second term. We thus obtain the cross section for the valley-orbit Raman process:

$$\frac{d^2\sigma}{d\Omega_R d\omega_R} = \left(\frac{e^2}{mc^2}\right)\frac{\omega_R}{\omega_L}\left(\frac{E_G^2}{E_G^2 - (\hbar\omega_L)^2}\right)^2$$

$$\times \left| \sum_{\alpha,\beta=1}^{3} (\lambda_L)_\alpha (\lambda_R^*)_\beta \sum_{j=1}^{N} \alpha_j^{(w)*}\alpha_j^{(v)} \right.$$

$$\times \left. \left[\left(\frac{m}{m^*}\right)_{\alpha\beta} - \delta_{\alpha\beta}\right]_j \right|^2 \delta(\omega - \omega_{n0}) . \quad (21)$$

Note that (e^2/mc^2) is r_0, the classical radius of the electron.

In a Raman experiment we can choose the laser and Raman polarization vectors. The cross section will be nonzero only if $[(m/m^*)_{\alpha\beta} - \delta_{\alpha\beta}]_j$ is also nonzero, and if the sum over j yields a non-zero result. Thus, the selection rules are determined by the orientation of the inverse effective-mass tensor with respect to the laser and Raman polarization vectors.

For process (ii) in which the state $|n\rangle$ is $|2s\rangle$ and the state $|0\rangle$ is the $|1s\rangle$ state, only the second term in expression (17) will contribute, with the result for $\sum_m$

$$\sum_m = 2\sqrt{2}\left(\frac{2}{3}\right)^4 \frac{m^* E_B^* E_G}{E_G^2 - (\hbar\omega_L)^2}$$

$$\times \sum_{\alpha,\beta=1}^{3} (\lambda_L)_\alpha (\lambda_R^*)_\beta \sum_j \alpha_j^{(w)*}\alpha_j^{(v)} . \quad (22)$$

The numerical coefficient in expression (22) is about 0.56. Thus, the ratio of the $\sum_m$ for process (2) to that of process (i) is about $0.56(m^*/m)(E_B^*/E_G)$.

In order to calculate the quantity $\sum_m$ for process (3) we keep the intermediate states in Eq. (10).

Saslow and Mills have considered such processes.[38] Using their results (and our approximations for the energy denominators), we obtain for a valley-orbit transition which proceeds via the $2p_z$ intermediate state a $\sum_m$ of about $0.23 m^*(E_B^*/\hbar\omega_L)^2$. For a $1s$ to $2s$ Raman transition with the $3p_z$ intermediate state, $\sum_m$ is about $5.4\times10^{-5} m^*(E_B^*/\hbar\omega_L)^2$. In calculating both of these terms we took $\alpha = \beta = z$. To obtain the ratio of these $\sum_m$ to that of process (i) we simply divide by the free-electron mass m; that is we approximate everything else as unity.

B. Coupled Phonon-Plasmon Modes

When a polar semiconductor is doped to degeneracy a plasma is obtained. The plasma oscillation is a long-wavelength electron-density oscillation, a longitudinal "vibrational mode" of the electron gas, and it can couple to the electric field of the long-wavelength LO phonon. The resulting mixed modes were first discussed by Varga[39] and may be found from the zeros of the real part of the total dielectric function $\epsilon(q \approx 0, \omega)$,

$$\frac{\epsilon(0, \omega)}{\epsilon_\infty} = \frac{\omega_{LO}^2 - \omega^2}{\omega_{TO}^2 - \omega^2} - \frac{\omega_P^2}{\omega(\omega + i/\tau)} . \quad (23)$$

The plasma frequency is given in terms of the electron density by

$$\omega_p = \left(\frac{4\pi n e^2}{m^*\epsilon_\infty}\right)^{1/2} . \quad (24)$$

A phenomenological damping time τ has been inserted in Eq. (23). The effects of damping on the mixed modes were first considered by Singwi and Tosi.[40]

There have been many theoretical and experimental studies of Raman scattering from these coupled modes. We give reference here only to some of the more recent publications.[41-44] Many of the theories show that the Raman cross section obeys

$$\frac{d^2\sigma}{d\Omega_R d\omega_R} \propto \mathrm{Im}\frac{1}{\epsilon(0, \omega)} . \quad (25)$$

Thus, we find

$$\frac{d^2\sigma}{d\Omega_R d\omega_R} \propto \frac{(\omega\tau)\omega_P^2(\omega^2 + 1/\tau^2)(\omega^2 - \omega_{TO}^2)^2}{(\omega\tau)^2[(\omega^2 + 1/\tau^2)(\omega^2 - \omega_{LO}^2) - \omega_P^2(\omega^2 - \omega_{TO}^2)]^2 + \omega_P^4(\omega^2 - \omega_{TO}^2)^2} , \quad (26)$$

where ω is the Raman frequency shift. Examination of this expression shows that the cross section is zero at zero frequency shift ($\omega = 0$) and at the TO phonon frequency ($\omega = \omega_{TO}$). Equation (26) is used in Sec. VII in an attempt to fit our observed shifted LO-phonon data.

V. RESULTS

The spectra for the sample having a nitrogen content of $\sim 1\times10^{17}/cm^3$ showed only those first-order

Raman-active phonons of 6H SiC that have been reported by Feldman et al.[22] In this section we present our new results for the nondegenerate (4×10^{18} SiC:N) and degenerate (6×10^{19} SiC:N) materials.

A. Results for SiC:N, $4\times10^{18}/cm^3$

Figure 2 shows the low-temperature Raman spectra for a sample having a nitrogen content of $4\times10^{18}/cm^3$. The power (P) in the figure caption has been corrected for losses due to the back-scat-
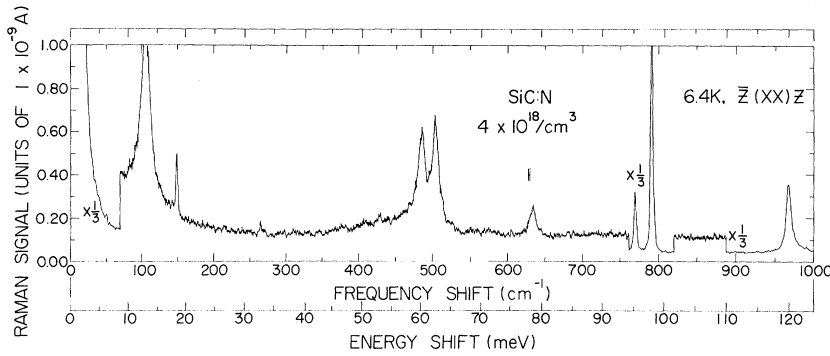
FIG. 2. The $\overline{Z}(XX)Z$ spectrum of $6H$ SiC:N, $4 \times 10^{18}/cm^3$ at 6.4 K ($P = 480$ mW). Note scale changes.

tering optics but not for losses due to the cryostat windows. Comparison with Table I shows that the new features of this spectrum are the appearance of peaks at 13.0 meV (105 cm^{-1}), 60.3 meV (486 cm^{-1}), 62.6 meV (505 cm^{-1}), and 78.8 meV (635 cm^{-1}). The depolarized $\overline{Z}(XY)Z$ spectrum (not shown), taken at the same temperature, shows the same modes,[45] thus indicating that all four peaks have E_2 symmetry. The sample having the resistivity of 0.14 Ω cm was used for back scattering off an $\overline{a}$ surface; the results showed that there were no A_1 or E_1 components to any of these four peaks.[45]

Figure 3 shows room-temperature data for the same sample that was used in taking the spectrum of Fig. 2. The 13.0-meV peak has disappeared. The two peaks at 60.3 and 62.6 meV have lost their distinction and appear as the single broad peak centered at 61.1 meV. The figure also shows that the 78.8-meV peak is observable, but has an asymmetric line shape. A room-temperature scan to energy shifts larger than those shown in Fig. 3 showed no new features.[45]

Careful scans of the planar acoustic E_2 doublet from $\chi = 0.33$ revealed another new feature. A high-resolution scan at 200 K, not shown here, of this doublet showed that the stronger peak was

asymmetric and exhibited a rapid drop in intensity on the high-energy side.[45] Figure 4 shows a photon-counting scan of this E_2-phonon doublet and of the 13.0-meV peak at 13 K. On the high-energy side of the large E_2-phonon peak, the signal drops below the signal due to the tail of the 13.0-meV peak, producing an interference effect. Figure 4 also shows the best fit we were able to obtain to a phenomonological model for the interference, which will be discussed in Sec. VI. Since the measured phonon linewidth was limited by instrumental resolution, it was necessary to convolute the theoretical line shape (dashed curve) with the instrumental profile. The result of this convolution is given by the solid line. Scans taken of the $\chi = 1.00$ planar acoustic E_2 phonon did not reveal an interference effect in this sample.[45]

The interference at the $\chi = 0.33$ planar acoustic E_2 doublet was very pronounced in the $6 \times 10^{19}/cm^3$ sample and apparently nonexistent in the $1 \times 10^{17}/cm^3$ sample. This can be seen from Fig. 5, which shows photon-counting data for all three samples. With increasing nitrogen content the higher-energy E_2 phonon shows a striking decrease in intensity relative to the lower-energy phonon, and both of the E_2 phonons shift to lower energy. For the $1 \times 10^{17}/$
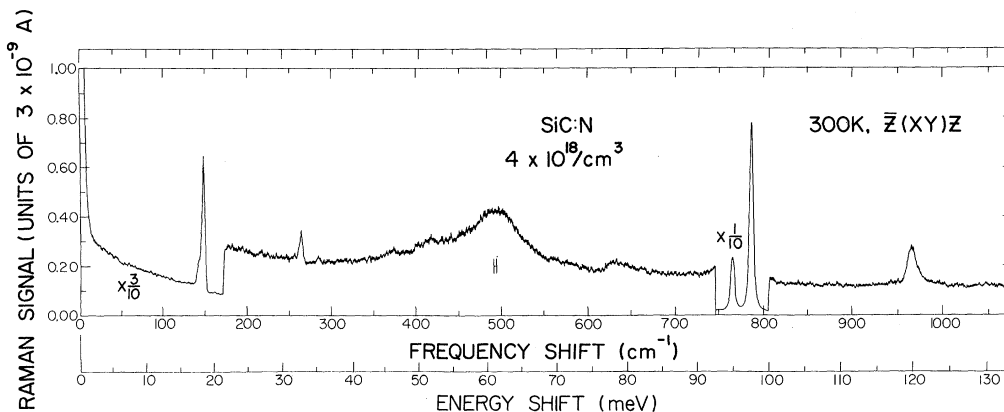
FIG. 3. The $\overline{Z}(XY)Z$ spectrum of $6H$ SiC : N, $4 \times 10^{18}/cm^3$ at 300 K ($P = 400$ mW). Note scale changes.
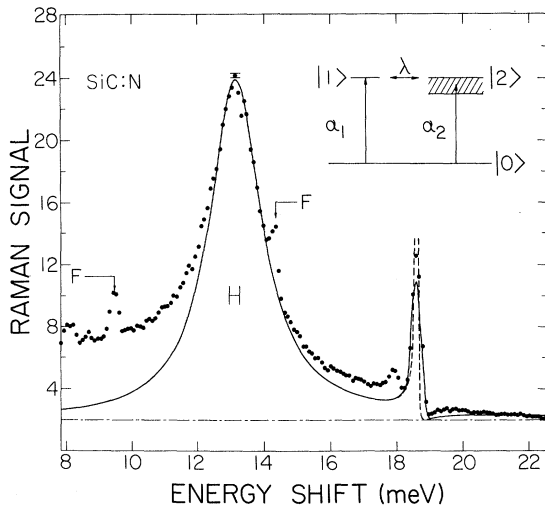
FIG. 4. The $\bar{Z}(XY)Z$ photon-counting spectrum of the 13.0-meV peak and the $\chi = 0.33$ planar acoustic E_2 doublet of $6H$ SiC:N, $4 \times 10^{18}/cm^3$ at 13 K ($P = 710$ mW). The black dots are the experimental points (units are 1000 counts in 10 sec). The dashed line is the theoretical calculation without convolution, and the solid line is the theoretical calculation convoluted with the instrumental profile. Peaks F are nonlasing fluorescence lines. The inset shows the phenomenological model used for the calculation.

cm^3 SiC : N sample the peaks are at 18.7 meV (150.4 cm^{-1}) and at 18.0 meV (144.9 cm^{-1}); for the $4 \times 10^{18}/cm^3$ sample, the minimum in the spectrum occurs at 18.9 meV (152.3 cm^{-1}), with peaks at 18.6 meV (149.8 cm^{-1}) and at 17.9 meV (144.0 cm^{-1}); for the $6 \times 10^{19}/cm^3$ sample the minimum is at 18.9 meV (152.3 cm^{-1}), and the peaks are at 18.4 meV (148.6 cm^{-1}) and at 17.8 meV (143.2 cm^{-1}).

Figure 6 shows the Raman spectra for the $15R$ SiC : N sample having a nitrogen content of $4 \times 10^{18}/cm^3$. The left-hand side of Fig. 6 shows two peaks at 7.7 meV (62 cm^{-1}) and 11.6 meV (94 cm^{-1}), although overlap of the peaks makes it difficult to determine the central energy. There are two shoulders at 2.5 meV (20 cm^{-1}) and 13.5 meV (109 cm^{-1}). The members of an E-phonon doublet occur at 20.8 meV (168 cm^{-1}) and 21.5 meV (173 cm^{-1}). The right-hand side of the figure shows peaks at 50.6, 54.9, 60.3, 62.8, 70.9, and 78.6 meV (408, 443, 486, 507, 572, and 634 cm^{-1}) and a shoulder at 46.0 meV (371 cm^{-1}).

B. Results for SiC : N, $6 \times 10^{19}/cm^3$

Figure 7 shows the depolarized spectrum at 9.8 K for the sample doped with 6×10^{19} nitrogen atoms per cm^3 for energy shifts less than 105 meV and the polarized spectrum for energy shifts greater than 105 meV. The 18.6-meV E_2 phonon is strongly interfering with the background. The 33.1-meV E_2 phonon, which showed no interference in the 4×10^{18}
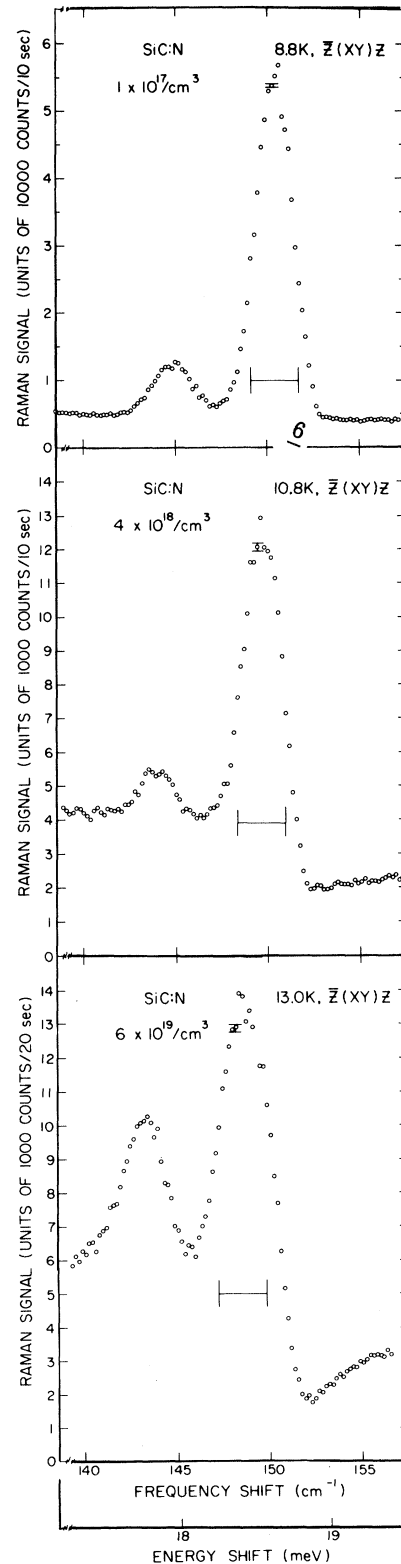
FIG. 5. The $\bar{Z}(XY)Z$ photon-counting spectrum of the $\chi = 0.33$ planar acoustic E_2 doublet of $6H$ SiC:N, $1 \times 10^{17}/cm^3$ at 8.8 K ($P = 710$ mW); $6H$ SiC:N, $4 \times 10^{18}/cm^3$ at 10.8 K ($P = 770$ mW); $6H$ SiC:N, $6 \times 10^{19}/cm^3$ at 13.0 K ($P = 500$ mW).
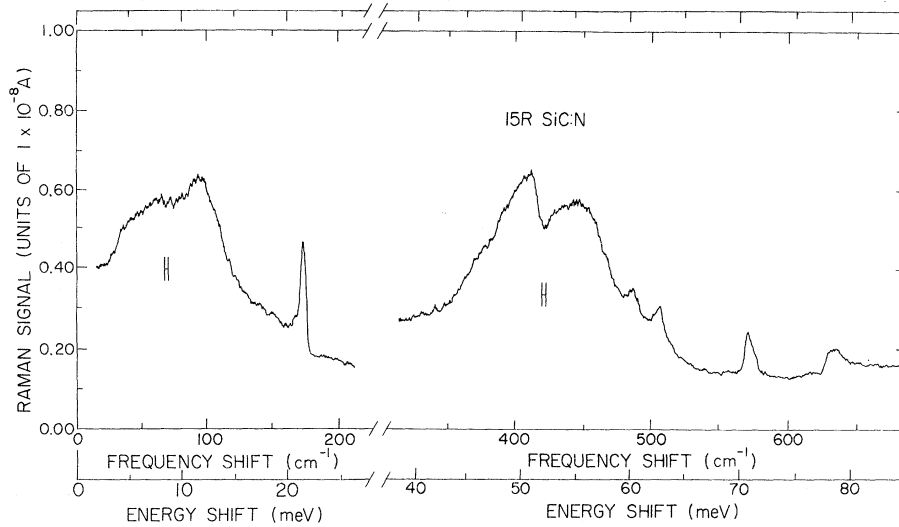
FIG. 6. Left-hand side: The depolarized spectrum of 15R SiC:N, $4 \times 10^{18}/cm^3$ at 15.6 K ($P = 360$ mW). Right-hand side: The unpolarized spectrum of 15R SiC:N, $4 \times 10^{18}/cm^3$ at 15.6 K ($P = 360$ mW).

SiC :N sample, now has an entirely dispersive character. There is a continuum extending to about 65 meV. The 78.8-meV mode of Fig. 2 appears at 79.6 meV (642 cm^{-1}); this peak shows a sharp onset but is asymmetric, and it is not possible to define its width. The polarized spectrum for energy shifts greater than 105 meV shows that the A_1(LO) phonon has shifted from 119.5 meV (964 cm^{-1}) to ~120.9 meV (975 cm^{-1}). This mode is asymmetric with a long tail on the high-energy side.

Figure 8 shows the depolarized spectrum at room temperature. The continuum has almost disappeared but its cutoff near 60–65 meV is still visible. The E_2 doublet from the point $\chi = 0.33$ on the planar acoustic branch and the $\chi = 1$ planar acoustic E_2 phonon are reduced in prominence from the low-temperature spectra. The 79.6-meV mode is not visible. A polarized spectrum (not shown here), taken at the same temperature, shows that the A_1(LO) phonon is still shifted and asymmetric, but is not as well defined as in the low-temperature data.[45] The continuum appears in the E_2– only $[\overline{Z}(XY)Z]$ geometry and thus has E_2 character. A

room-temperature scan on an $\vec{a}$ surface of this sample showed that there was no E_1 component to the continuum. In addition, these same scans showed that the shifted A_1(LO) mode obeyed the usual selection rules for an A_1(LO) phonon; that is, no mode was observed for back scattering off the $\vec{a}$ surface.

The insert in Fig. 8 gives a high-resolution scan of the $\chi = 0.33$ planar acoustic E_2 doublet at room temperature. This spectrum shows an interference involving the smaller E_2-phonon peak at this concentration, whereas it did not show an interference for the 4×10^{18} sample.

Photon-counting data on the shifted LO phonon are presented in Fig. 9. Figure 9(a) shows the actual data. We have drawn a baseline through the data points, which is consistent with the sloping background observed in the $\overline{Z}(XY)Z$ spectrum in this region. In Fig. 9(b) we have subtracted the baseline from the data of Fig. 9(a). The solid line is a theoretical fit to be described in Sec. VII.

Finally, we mention that spectra were taken for several other samples from lot 634, including a
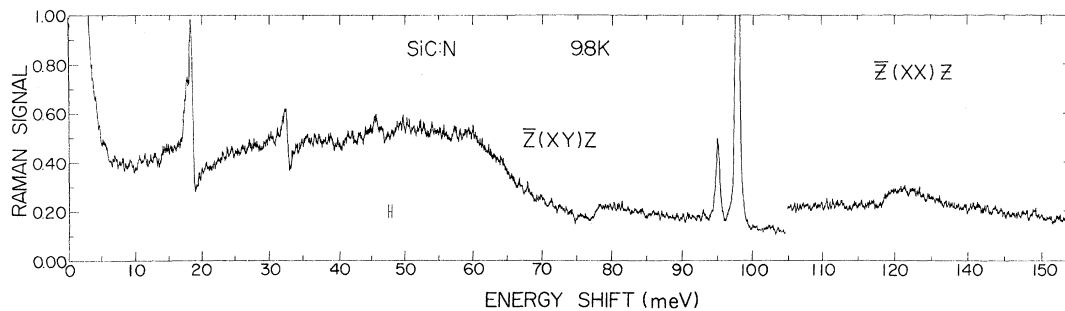
FIG. 7. The $\overline{Z}(XY)Z$ spectrum of 6H SiC:N, $6 \times 10^{19}/cm^3$ at 9.8 K ($P = 770$ mW) for energy shifts less than 105 meV, and the $\overline{Z}(XX)Z$ spectrum for energy shifts greater than 105 meV.
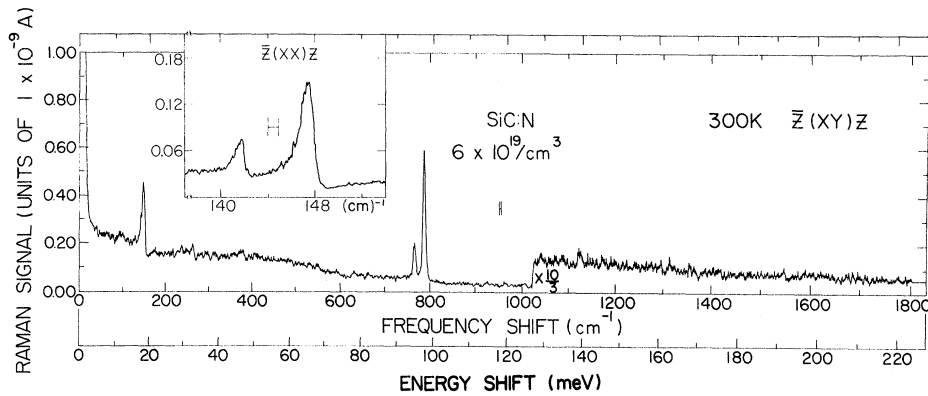
FIG. 8. The $\bar{Z}(XY)Z$ spectrum of 6H SiC:N, $6 \times 10^{19}/cm^3$ at 300 K ($P = 540$ mW). The inset gives a high-resolution scan of the $\chi = 0.33$ planar acoustic E_2 doublet.

sample on which metal-insulator-semiconductor (M-I-S) tunneling had been performed,[26] in order to see whether the interference effect between the continuum and E_2 phonons occurred in all samples. All samples showed this interference effect at room temperature. The strength of the interference, however, varied from sample to sample. Spectra were taken at low temperatures on the sample which had been used in M-I-S tunneling. The E_2 continuum was better defined, for this sample, than the room-temperature data of Fig. 8, but not as well defined as the low-temperature data of Fig. 7. The interference effect with the E_2 phonons was clearly observable, but it was not as pronounced as in Fig. 7.

VI. DISCUSSION FOR SiC:N, $4 \times 10^{18}/cm^3$

A. Valley-Orbit Raman Transitions

We attribute the 13.0-, 60.3-, and 62.6-meV peaks to $1s(A_1) \rightarrow 1s(E)$ valley-orbit transitions of the donor electron at the three inequivalent sites. The temperature dependence of the modes shows that complete thermalization of the 13.0-meV peak has occurred at room temperature, and a partial but significant thermalization has occurred for the 60.3- and 62.6-meV peaks (Figs. 2 and 3). This temperature dependence suggests that these modes are due to electronic transitions rather than to possible resonance modes of the impurity.

With the results derived in Sec. VI we can show that the most likely electronic Raman processes that can occur for shallow donors in an indirect-gap semiconductor are valley-orbit transitions. Consider the relative strengths of the valley-orbit matrix element [process (i) of Sec. IV A] and the next most likely process, namely $1s \rightarrow 2s$ [process (ii) of Sec. IV A]. The ratio of the matrix elements ($\sum_m$) of the $1s \rightarrow 2s$ transition which proceeds via the valence-band intermediate state to the valley-orbit matrix element was shown to be $0.56(m^*/m)(E_B^*/E_G)$. For 6H silicon carbide we take $E_G(\vec{k}_j)$ as 4.0 eV, since we expect the direct gap at $\vec{k}_j$ to be sig-

nificantly higher than the 3.024-eV exciton energy gap. If we use a binding energy of 0.20 eV (which was one of the ionization energies obtained by Choyke and Patrick[2]), and take (m^*/m) as $\frac{1}{2}$, then the ratio of the matrix elements is about 1.4×10^{-2}. The ratio of the cross sections is then about 2×10^{-4}.

If the $1s \rightarrow 2s$ transition proceeded via the $3p_z$ hydrogenic state [process (iii) of Sec. IV A], the ratio of this matrix element to the valley-orbit matrix element is about 8.2×10^{-4} and the ratio of cross sections is about 6.7×10^{-7}.

These estimates show that it is highly unlikely that the electronic Raman transitions that we observe are anything but valley-orbit Raman transitions. Moreover, the second term of Eq. (20) is $\frac{1}{30}$ of the first term of Eq. (20), and thus produces a cross-section ratio of about 10^{-3}. Thus, the cross section will be given by expression (21) and
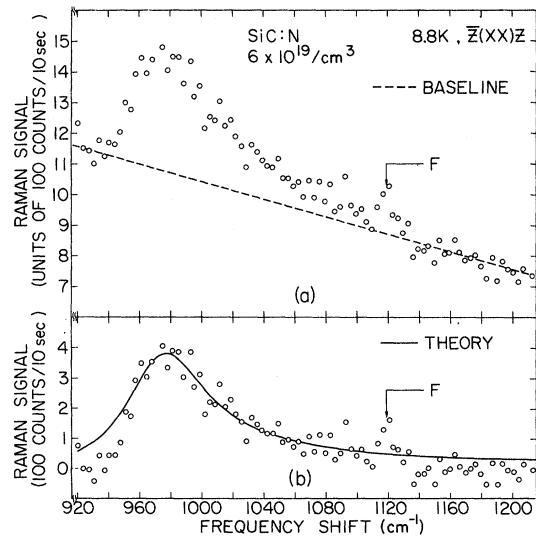
FIG. 9. (a) $\bar{Z}(XX)Z$ photon-counting spectrum of the shifted $A_1(LO)$ phonon of 6H SiC:N, $6 \times 10^{19}/cm^3$ at 8.8 K ($P = 770$ mW). (b) The shifted $A_1(LO)$ phonon with the baseline of part (a) (dashed line) subtracted and the fit to theory (solid line).

the selection rules determined by the orientation of the inverse-effective-mass tensor with respect to the laser and Raman polarization vectors.

We know from Woodbury and Ludwig's ESR results that the ground state of the donor-electron wave function is isotropic,[5] and we conclude from this that the $1s(A_1)$ state is the ground state of the valley-orbit split levels. The other state allowed by the C_{3v} donor-site symmetry is $1s(E)$, which we take to be the upper state of the transition. The Raman transition should thus have E symmetry, which is a mixture of E_1 and E_2. Our measurements showed that the transition had E_2 symmetry only. This significant result, which allows the assignment of possible locations of the conduction-band minima, is discussed below.

We assume that the three peaks arise from valley-orbit transitions occurring at nitrogen donors located on the three inequivalent sites. Moreover, we suggest that the 60.3- and 62.6-meV transitions occur for donors on the two cubic sites, and the 13.0-meV transition for donors on the hexagonal site. These assignments are in qualitative agreement with Choyke and Patrick's observation of three phonon-free lines in the emission spectra.[1] Two of the phonon-free lines had the same intensity, and were very close in energy. With their equal intensity and closeness in energy the 60.3- and 62.6-meV peaks show the same qualitative behavior. The third phonon-free line was quite different in energy and intensity from the other two lines, and we note that the 13.0-meV peak shows the same behavior. The observation of the equal intensities of two of the transitions is also in agreement with Woodbury and Ludwig's conclusion that two of the sites give essentially the same ESR behavior.[5]

We recall that Patrick assigned the two similar phonon-free lines to recombination of the exciton bound to nitrogen on the two cubic sites and the other line to the hexagonal site.[3] It should not be confusing that the hexagonal phonon-free line has a smaller intensity than the cubic phonon-free lines, whereas the hexagonal Raman peak is roughly twice as intense as either of the cubic transitions, since recombination radiation and valley-orbit Raman transitions are quite different phenomena.

Observation of the valley-orbit splitting in other SiC polytypes would offer a method for checking our assignments of the larger valley-orbit splittings to nitrogen on the cubic sites and the smaller splitting to nitrogen on the hexagonal sites. Nitrogen-doped cubic SiC, which has the zinc-blende lattice and C_{3v} site symmetry, should show one valley-orbit transition with an energy closer to 60 than to 13 meV. Hartman and Dean estimated the valley-orbit splittings as ~60 meV for cubic SiC:N.[46] They arrived at this value by subtracting the effective-mass donor ionization energy ~40 meV from the approximate

experimental ionization energy ~100 meV.[47]

In an attempt to verify the cubic- and hexagonal-site assignments in 6H SiC:N we have observed the valley-orbit splittings in 15R SiC:N. The 15R polytype has two hexagonal and three cubic sites.

We believe the two peaks (Fig. 6) at about 7.7 and 11.6 meV result from transitions of those donors that are located on the two hexagonal sites, and the 50.6- and 54.9-meV peaks to donors on two of the three cubic sites. The 13.5-, 60.3-, and 62.8-meV peaks are best assigned as the 6H valley-orbit transitions due to mixing of the 6H polytype in the 15R polytype. This is a common occurrence since 6H is the preferred polytype, and our sample, in particular, had one edge that was composed of 6H SiC:N. The 2.5-meV shoulder is due to a nonlasing fluorescence line. The 78.6-meV peak is very close in energy to the 78.8-meV mode observed in 6H SiC:N. This leaves the shoulder at 46.0 meV and the peak at 70.9 meV as candidates for the fifth valley-orbit transition. Since the 46.0 meV shoulder is closest in energy to the 50.6- and 54.9-meV transitions, it is more likely to be the fifth transition. Thus 15R SiC:N shows two energy groupings of the valley-orbit transitions due to donors on the five inequivalent sites. The smaller valley-orbit splittings 7.7 and 11.6 meV are most likely due to $1s(A_1) \rightarrow 1s(E)$ transitions at the two hexagonal donor sites and the larger valley-orbit splittings 50.6, 54.9, and possibly 46.0 meV to the three cubic sites.

It is possible that this assignment of the large (small) valley-orbit splittings to donors on the cubic (hexagonal) sites is too simple an explanation. Patrick has pointed to the fact that the energies of the phonon-free lines observed in edge emission seemed to fit into cubic- and hexagonal-site groupings until the phonon-free lines were measured for 21R SiC:N and were found not to fit the expected groupings. Patrick suggested that the Kohn-Luttinger interference effect might be responsible for the observed energy groupings, and demonstrated this for 4H SiC:N.[48] We believe that Raman scattering from nitrogen in other SiC polytypes would demonstrate whether or not a similar situation applies for valley-orbit transitions.

What is significant about the valley-orbit transitions in both 6H and 15R SiC:N is the wide energy separation between the low-energy region (the 7.7-, 11.6-, and 13.0-meV transitions) and the high-energy region (the 46.0-, 50.6-, 54.9-, 60.3-, and 62.6-meV transitions). These large differences in valley-orbit splittings for donors on the inequivalent sites are due to extended departures of the impurity potential from the effective-mass potential $(-e^2/\epsilon_0 r)$ to which the various ground- and excited-state wave functions are sensitive. This sensitivity has been recently demonstrated by Patrick by consider-

ing the effects of the interference factors $e^{i\vec{k}\cdot\vec{r}_j}$ in Eqs. (12) and (13).[49]

B. Location of the Conduction-Band Minima

In Sec. IV A it was shown that the symmetry of the valley-orbit transitions depends on the components of the inverse-effective-mass tensor $(m/m*)_{\alpha\beta}$. While the coefficients $\alpha_j^{(v)}$ depend on the site symmetry and, thus, will have A_1 and E symmetry, we have seen that the valley-orbit transitions occur experimentally only for E_2 polarization geometries and not for the (XZ) and $(YZ) E_1$ polarization geometries. This means that the XZ and YZ components of the inverse-effective-mass tensor must be zero.

We also note that we observe only one transition per hexagonal or cubic donor site. Neglecting doubling due to time-reversal invariance (minima coupled only by time reversal will not show a valley-orbit splitting), if there were six (twelve) conduction-band minima we would expect two (four) A_1 levels and two (four) E levels per site. Both the E_2 symmetry and the fact of a single transition per site can be explained if the conduction-band minima lie along the edges of the lines ML (the mirror planes) in the Brillouin zone. If the minima are at either M or L points there would be one $1s(A_1)$ and one $1s(E)$ transition per site. For minima lying along ML the three minima lying above the basal plane are connected with the three below by time reversal only, and there will, again, be one $1s(A_1)$ level and one $1s(E)$ level per donor site. It can be shown, also, that E states made up from Bloch functions on ML transform like E_2 under C_{6v} operations.[49] Thus, the $1s(A_1) \rightarrow 1s(E)$ transitions would have pure E_2 Raman symmetry. This location of the conduction-band minima on ML is consistent with the location by Junginger and van Haeringen[20] and Herman *et al.*[21] of the conduction-band minima at the M point.

C. Resonant-Interference Effect

When the energy and symmetry of a discrete level coincides with the energy and symmetry of a continuum, and when there is a term in the Hamiltonian that mixes the discrete and continuum states then the discrete level may undergo a "radiationless transition" to the continuum. Such processes are also called "Auger processes" or "resonant interference." Fano has pointed out that the discrete level will manifest itself as an asymmetric peak, because in mixing the discrete and continuum states to form a stationary state of energy E, the coefficients vary sharply when E passes through the discrete level.[50] This also results in the transition probability going to zero at a certain energy; thus a dip will appear in the spectrum. These features are exhibited by the asymmetric line shape of the

18.6-meV E_2 phonon and the dip at 18.9 meV as shown by Figs. 4, 5, 7, and 8.

In solving an interference problem in quantum mechanics it is necessary to add amplitudes before squaring (in the golden rule), and this means that the interference is a manifestation of phase coherence. Fano[50] and Fano and Cooper[51] have given a quantum-mechanical description of Auger processes.

For the 4×10^{18} SiC:N sample the question of the identity of the continuum arises. Moreover, if a continuum were clearly observable the Fano formulation will allow a fit to the line shape of the discrete level but will not shed light on what the continuum is. We now propose a model for the interference effect observed in the Raman spectra of the 4×10^{18} SiC:N sample. It assumes that the observed $1s(E_2)$ electronic level at 13.0 meV mixes with the 18.6-meV E_2 phonon.

The insert in Fig. 4 shows the model used to obtain the fit. We assume that the first excited state of the E_2 phonon is coupled via a real electron-phonon coupling constant λ to the $1s(E)$ valley-orbit level. The excited phonon is labeled by the state $|1\rangle$, and the $1s(E)$ excited donor level by the state $|2\rangle$. The ground state is denoted by $|0\rangle$. The creation of the phonon via the Raman process is described by the polarizability tensor $\alpha_1\vec{\epsilon}$, and the Raman transition to the $1s(E)$ level is described by $\alpha_2\vec{\epsilon}$. Here α_1 and α_2 are assumed to be real parameters, and $\vec{\epsilon}$ is a tensor representation of E_2. For example, $\vec{\epsilon}$ may be chosen to have (xy) elements equal to unity and all others equal to zero, or it may be chosen to have elements given by $(xx) = -(yy) = -1$ and all others equal to zero. The over-all Raman transition is then described by the tensor operator

$$\vec{\alpha}_{op} = \alpha_{op}\vec{\epsilon}, \tag{27}$$

$$\alpha_{op} = \alpha_1[|0\rangle(1| + |1\rangle(0|] + \alpha_2[|0\rangle(2| + |2\rangle(0|] . \tag{28}$$

The low-temperature Stokes-Raman intensity for a given E_2 polarization geometry $[(XX), (YY)$, or $(XY)]$ will be proportional to the transition rate ($\hbar = 1$ here):

$$W(\omega) = 2\pi\sum_n |\langle n|\alpha_{op}|0\rangle|^2 \delta(E_n - \omega)$$
$$= -2\,\text{Im}\langle 0|\alpha_{op}^\dagger(H - \omega + i\eta)^{-1}\alpha_{op}|0\rangle, \quad (\eta = 0^+). \tag{29}$$

With the zero of energy corresponding to the ground state, the Hamiltonian is given by $H = H_0 + H'$:

$$H_0 = \omega_0|1\rangle(1| + \Omega_0|2\rangle(2| , \tag{30}$$
$$H' = \lambda[|1\rangle(2| + |2\rangle(1|] ,$$

where, for now, we assume that both the phonon energy ω_0, and the electronic excitation energy Ω_0,

are sharply defined. Equation (29) may be rewritten in terms of the matrix elements of the resolvent operator $R(z) \equiv (H - z)^{-1}$ as follows:

$$W(\omega) = 2\,\text{Im} \sum_{i,j=1}^{2} (0\,|\,\alpha_{op}^{\dagger}\,|\,i)(i\,|\,R(z)\,|\,j)(j\,|\,\alpha_{op}\,|\,0)$$

$$= -2\,\text{Im} \sum_{i,j=1}^{2} \alpha_i \alpha_j (i\,|\,R\,|\,j)\,, \quad z = \omega - i\eta\,. \quad (31)$$

The matrix elements are readily found to be

$$(1\,|\,R\,|\,1) = (\Omega_0 - z)/D\,,$$

$$(1\,|\,R\,|\,2) = (2\,|\,R\,|\,1) = -\lambda/D\,, \quad\quad\quad (32)$$

$$(2\,|\,R\,|\,2) = (\omega_0 - z)/D\,,$$

$$D = (\omega_0 - z)(\Omega_0 - z) - \lambda^2\,.$$

To treat the finite width of the 13-meV electronic transition, we let Ω_0 be complex, $\Omega_0 \to \Omega_0 + i\gamma$, write $\alpha_2 = \alpha_1 \delta$, and obtain finally for the Raman transition rate

$$W(\omega) = \frac{2\alpha_1^2 \gamma [\lambda - (\omega_0 - \omega)\delta]^2}{[(\omega_0 - \omega)(\Omega_0 - \omega) - \lambda^2]^2 + \gamma^2(\omega_0 - \omega)^2}\,. \quad (33)$$

Note that the numerator of Eq. (33) may vanish at a certain energy, $\omega_m = \omega_0 - \lambda/\delta$, producing a dip in the spectrum. The parameters used for the fit shown in Fig. 4 are as follows: $\gamma = 0.97$ meV, $\lambda = 1.00$ meV, $\omega_0 = 18.78$ meV, $\Omega_0 = 12.97$ meV, and $\delta = 22$.

This interference between a nonpolar phonon state and a $1s(E_2)$ donor level is a new effect. It is formally similar to interferences between two phonon states that have been reported in the literature.[52-54]

D. Vibrational Mode

Figure 2 showed a mode occurring at 78.8 meV. This mode has also been observed in metal-insulator-semiconductor tunneling by Schein and Compton.[26] We have previously reported these results.[55] The fact that this peak was seen in M-I-S tunneling led us to conclude that we were observing a vibrational mode, since donor electronic levels are not observable in M-I-S measurements. Our results on 15R SiC : N (Fig. 6) showed a mode at 78.6 meV which is very close in energy to the 78.8-meV mode in the 6H material. The estimated donor ionization energies in 15R SiC : N suggest that the effective mass of 15R SiC is smaller than that of 6H SiC.[56] Thus the 78.6-meV value is independent of changes in the effective mass while the energies of the valley-orbit transitions are not. This tends to confirm the vibrational character of this mode.

VII. DISCUSSION FOR SiC:N, 6×10^{19}/cm^3

A. Resonant Interferences

Figures 7 and 8 showed that three of the host-crystal E_2 phonons interfered with the continuum,

which extended to about 60–65 meV. Low-temperature photon-counting data (not shown here) were taken on the $\chi = 0.33$ planar acoustic E_2 doublet.[45] We attempted to fit the data for the larger member of this doublet to our model for the interference occurring in the 4×10^{18} sample; the energy of the electronic mode was set to zero in the computation, while its width and the electron-phonon coupling constant were varied. We were able to fit the peak height of the phonon and to obtain a fair fit to the high-energy side of the mode. The values of the fit intensity on the low-energy side of the phonon were much greater than the data points. This shows, along with the insert of Fig. 8, that both members of the doublet interfere with the continuum at this concentration. This preliminary fit also showed that the entire continuum in the 18.9-meV region is involved in the interference, since the minimum in the theoretical curve without convolution had about zero intensity–the nonzero nature of the observed minimum resulted from the finite resolution of the monochrometer. Finally, the 33.1-meV E_2 phonon was fit to the Fano formalism[50] and was shown to be entirely dispersive relative to the continuum.

We note that the strength of the interference is quite temperature dependent, being strong at low temperature and weak at room temperature. This appears to correlate with the strength of the continuum which is strong and well defined at low temperatures and weak at room temperature.

B. Continuum

Figure 7 showed a continuum which had E_2 symmetry, interfered with host-crystal E_2 phonons, and extended to 60–65 meV. Spin-density fluctuations[57] and nonparabolic scattering mechanisms[58] for single-particle excitations of electrons out of the Fermi sea can be ruled out as possible explanations for the continuum on the basis of the energy cutoff that these mechanisms have. They both have a maximum energy of the wave vector transferred (q) times the Fermi velocity (v_F). For a total of three (six) conduction-band minima, qv_F is 5.2 meV (4.2 meV), for a plasma frequency of 86.8 meV (see below). In addition neither of these mechanisms can account for the E_2 symmetry of the continuum.

We believe the properties of the continuum can be explained if we assume that the donor-electron wave functions have retained some local character even though the metallic transition[7,12] is known to occur at 2×10^{19} nitrogen donors/cm^3. In particular, we assume that we are still observing $1s(A_1)$ $\to 1s(E)$ transitions, but that both levels are now broadened to the point where they overlap, since the continuum starts at zero excitation frequency. The E_2 symmetry is explained by the fact that the

$1s(A_1) \rightarrow 1s(E)$ transitions have E_2 symmetry due to the location of the conduction-band minima along the line ML in the Brillouin zone. Since the final state of the 13.0-meV transition was shown to interfere with an E_2 phonon in the sample having a nitrogen content of $4 \times 10^{18}/cm^3$, it is expected that the final state of these broadened valley-orbit levels can interfere with E_2 phonons. Finally, we note that two of the valley-orbit transitions in the 4×10^{18} sample occurred at energies (60.3 and 62.6 meV) in the region where the continuum cuts off.

We recall that Alexander's,[10] Hardeman's,[9] and van Wieringen's[6] results were not characteristic of metallic electrons. Our Raman results offer another method for observing this unusual behavior of shallow donors in a semiconductor. The NMR and ESR results were observed for electrons in the ground state, while the Raman measurements leave the electrons in their excited state, and we observe a convolution of the broadened $1s(A)$ density of states with the broadened $1s(E)$ density of states.

C. Coupled LO-Phonon–Plasmon Mode

At the same time that we believe that the continuum discussed above is not characteristic of delocalized electrons, we believe that this sample shows some delocalized properties, since we interpret the shifted asymmetric LO phonon shown in Fig. 9 as the L^+-coupled LO-phonon–plasmon mode. Figure 9(b) shows the fit of Eq. (26) to the data. The following parameters were used for the fit:

$$\omega_P = 700 \text{ cm}^{-1} \quad (86.8 \text{ meV}) \, ,$$

$$1/\tau = 2400 \text{ cm}^{-1} \quad (297.5 \text{ meV}) \, ,$$

$$\omega_{LO} = 964 \text{ cm}^{-1} \quad (119.5 \text{ meV}) \, , \tag{34}$$

$$\omega_{TO} = 788 \text{ cm}^{-1} \quad (97.7 \text{ meV}) \, .$$

The electron collision lifetime τ is thus 2.2×10^{-15} sec.

The figure shows that the fit deviates significantly from the data in the 940-cm^{-1} region. Indeed, since the data drop sharply below the calculated curve, some additional interference mechanism may be operating. Since the $A_1(LO)$ phonon is normally allowed in this $\overline{Z}(XX)Z$ geometry, both the deformation potential and electrooptic mechanisms for the coupling of light to electrons can contribute to the cross section. A theory which included both these coupling mechanisms gave a better fit in the 940-cm^{-1} region. This theory and the fit to the data will be discussed elsewhere.[59]

In spite of the fact that Eq. (26) does not give the entire frequency dependence, some significant qualitative features concerning the L_+ mode may be derived from our fit. The important point about the parameters used is that the electron-collision

lifetime is very short. This results in a highly damped L_+ mode and produces the asymmetric line shape. Moreover, our inability to detect the L_- mode stems from this damping. The damping also has the effect of keeping the L_+ mode closer in energy to the LO phonon than would be calculated from the electron concentration with no damping.

These features are demonstrated in Fig. 10, which shows the entire spectrum of Eq. (26) for the parameters given above. (Here, we have omitted the normalization constant which was used for the theoretical curve of Fig. 9.) The small cross section in the 0–800-cm^{-1} region shows why we were unable to detect the L_- mode of the coupled LO-phonon–plasmon system.

From the values of ω_P (700 cm^{-1}), $1/\tau$ (2400 cm^{-1}), an assumed electron effective mass of $m^* = \frac{1}{2} m_0$, an assumed number of conduction-band minima of $N = 3(6)$, and an average high-frequency dielectric constant of $\epsilon_\infty = (\epsilon_\infty^{||} \epsilon_\infty^{\perp})^{1/2} = 6.61$, we can calculate several quantities of the electron gas which will be useful in subsequent discussions. These quantities are given as follows:

$$n(\text{free-electron density}) = \frac{\epsilon_\infty m^* \omega_P^2}{4\pi e^2}$$

$$= 1.7 \times 10^{19}/cm^3 \, ,$$

$$k_F(\text{Fermi wave vector}) = \left(\frac{3\pi^2 n}{N}\right)^{1/3}$$

$$= 5.5(4.4) \times 10^6 \text{ cm}^{-1} \, ,$$

$$\omega_F(\text{Fermi frequency}) = \frac{\hbar}{2m^*} k_F^2 = 23.0(14.5) \text{ meV} \, ,$$

$$v_F(\text{Fermi velocity}) = \frac{\hbar k_F}{m^*} = 1.3(1.0) \times 10^7 \text{ cm/sec} \, ,$$

$$k_{F\text{-}T}(\text{Fermi-Thomas wave vector}) = \left(\frac{6\pi n e^2}{\hbar \omega_F}\right)^{1/2}$$

$$= 4.5(5.6) \times 10^7 \text{ cm}^{-1} \, ,$$

$$\mu(\text{dc mobility}) = \frac{e\tau}{m^*} = 7.7 \text{ cm}^2/\text{V sec} \, ,$$

$$\Lambda(\text{mean free path}) = v_F \tau = 2.9(2.3) \text{ Å} \, .$$

We used the calculated electron density in obtaining
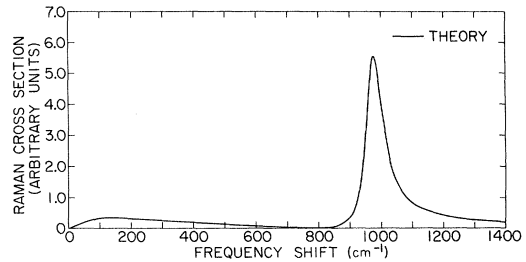
FIG. 10. Calculation of Eq. (26) for $\omega_P = 700$ cm^{-1}, $1/\tau = 2400$ cm^{-1}, $\omega_{LO} = 964$ cm^{-1}, and $\omega_{TO} = 788$ cm^{-1}.

the Fermi wave vector, the Fermi-Thomas wave vector, and quantities deriving from k_F and k_{F-T}. These quantities should be considered as approximate results in view of the assumptions made concerning m^* and N.

The value of the calculated mobility agrees well with the Hall mobility, obtained by Lely and Kröger[7] and Violina et al.,[12] of ~10 cm^2/V sec for samples with a nitrogen content of 2×10^{19}/cm^3 or larger.

VIII. SUMMARY

Our results for Raman measurements on nondegenerate nitrogen-doped silicon carbide can be summarized as follows.

(a) Valley-orbit transitions $[1s(A_1) \rightarrow 1s(E)]$ were observed for donors on inequivalent sites in $6H$ and $15R$ SiC. These transitions were grouped into two widely separated energy regions, showing that the donor wave functions are very sensitive to the details of the impurity potential beyond the central cell. The assignment of the transitions to donors on the inequivalent sites correlates with luminescence results and ESR results.[1, 2, 4, 5]

(b) The Raman symmetry of the valley-orbit transitions was E_2. This fact was used to show that the conduction-band minima lie along the line ML in the Brillouin zone. There are three minima if they are at either M or L point and six if they are at a general point along ML. This conclusion is consistent with calculations of the minima as being at the M point,[20, 21] although the calculations are probably not accurate enough for a definite assignment to be made. Patrick has argued that the Kohn-Luttinger interference effect can explain the site dependences of the $1s$ A-E splittings and exciton binging energies only if the minima are at a general point on ML.[49]

(c) A resonant interference effect was observed to occur with a host-crystal E_2 phonon. A fit to the line shape of this effect was obtained with the use of a model that assumed that the excited state of one of the valley-orbit transitions mixed with the

E_2-phonon state.

(d) A mode which occurred in all samples (degenerate and nondegenerate) at approximately the same energy was correlated with observation of a peak occurring at the same energy in M-I-S tunneling. Since this peak appeared in tunneling and was independent of changes in the effective mass of the $6H$ and $15R$ host crystals, it was interpreted as being vibrational in character.

Our results for degenerate $6H$ silicon carbide were the following.

(1) A "continuum" was observed which resonantly interfered with several E_2 phonons. The continuum was conjectured to result from broadened and overlapping $1s(A_1)$ and $1s(E_2)$ valley-orbit levels, since it had the same symmetry and resonant interference properties as the valley-orbit transitions, and since its cutoff was in the region of two of the valley-orbit transitions in the nondegenerate sample. This result was considered to be nonmetallic in the sense that the continuum could not be explained as arising from single-particle excitations out of the Fermi sea. This adds to the pieces of evidence from NMR and ESR that degenerate SiC shows some nonmetallic behavior.

(2) Our data showed a shifted asymmetric LO phonon which was interpreted as a coupled LO-phonon–plasmon mode (L^+). This result is characteristic of a metallic system, and the calculated mobility agrees with values measured on heavily doped samples. The asymmetry of the mode and the absence of the L^- LO-phonon–plasmon mode was largely due to a short electron-collision lifetime.

ACKNOWLEDGMENTS

*Work supported in part by the Advanced Research Projects Agency, under Contract No. HC 15-67-C-0221.

*Present address: James Franck Institute, The University of Chicago, Chicago, Ill. 60637.

[1]W. J. Choyke and L. Patrick, Phys. Rev. 127, 1868 (1962).

[2]D. R. Hamilton, W. J. Choyke, and L. Patrick, Phys. Rev. 131, 127 (1963).

[3]L. Patrick, Phys. Rev. 127, 1878 (1962).

[4]J. S. Gorban, A. F. Gumenyuk, and Yu. M. Suleimanov, Fiz. Tverd. Tela 8, 3424 (1966) [Sov. Phys. Solid State 8, 2746 (1967)].

[5]H. H. Woodbury and G. W. Ludwig, Phys. Rev. 124, 1083 (1961).

[6]J. S. van Wieringen, in Semiconductors and Phosphors: Proceedings of the International Colloquium, 1956, in Garmisch-Partenkirchen, edited by M. Schön and H.

Welker (Interscience, New York, 1958), p. 367.

[7]J. A. Lely and F. A. Kröger, in Ref. 6, p. 525.

[8]M. I. Iglitsyn, I. I. Ivanova, G. E. Konstantinova, M. G. Kosaganova, N. V. Osyannikova, N. M. Pavlov, and E. E. Fedotova, in Silicon Carbide, edited by Academician I. N. Frantsevich (Consultants Bureau, New York, 1970), p. 48.

[9]G. E. G. Hardeman, J. Phys. Chem. Solids 24, 1223 (1963).

[10]M. N. Alexander, Phys. Rev. 172, 331 (1968).

[11]M. N. Alexander and D. F. Holcomb, Rev. Mod. Phys. 40, 815 (1968).

[12]G. N. Violina, Yeh Liang-hsiu, and G. F. Kholuyanov, Fiz. Tverd. Tela 5, 3406 (1963) [Sov. Phys. Solid State 5, 2500 (1964)].

[13]S. H. Hagen and C. J. Kapteyns, Philips Res. Repts. 25, 1 (1970).

[14] H. J. van Daal, Philips Res. Repts. Suppl. 3, 70 (1965).

[15] P. J. Colwell and M. V. Klein, in *Light Scattering in Solids*, edited by M. Balkanski (Flammarion Sciences, Paris, 1971), p. 102.

[16] W. J. Choyke and L. Patrick, Phys. Rev. 105, 1721 (1957).

[17] B. Ellis and T. S. Moss, Proc. Roy. Soc. (London) 299, 383 (1967).

[18] W. J. Choyke, D. R. Hamilton, and L. Patrick, Phys. Rev. 139, A1262 (1965).

[19] L. Patrick, W. J. Choyke, and D. R. Hamilton, Phys. Rev. 137, A1515 (1965).

[20] H. G. Junginger and W. van Haeringen, Phys. Status Solidi 37, 709 (1970).

[21] F. Herman, J. P. Van Dyke, and R. L. Kortum, in *Silicon Carbide-1968*, edited by H. K. Henisch and R. Roy (Pergamon, New York, 1969), p. S167 (published as a special issue of Materials Research Bulletin, Vol. 4.)

[22] D. W. Feldman, J. H. Parker, Jr., W. J. Choyke, and L. Patrick, Phys. Rev. 170, 698 (1968).

[23] C. H. Hodges, Phys. Rev. 187, 994 (1969).

[24] D. W. Feldman, J. H. Parker, Jr., W. J. Choyke, and L. Patrick, Phys. Rev. 173, 787 (1968).

[25] L. B. Schein (private communication, 1970).

[26] L. B. Schein, Ph. D. dissertation (University of Illinois, Urbana, 1970) (unpublished); L. B. Schein and W. D. Compton, Appl. Phys. Letters 17, 326 (1970).

[27] G. A. Slack and R. I. Scace, J. Chem. Phys. 42, 805 (1965).

[28] R. L. Rosenbaum, Rev. Sci. Instr. 39, 890 (1968); 40, 577 (1969).

[29] P. J. Colwell and M. V. Klein, Solid State Commun. 8, 2095 (1970).

[30] H. Poulet, Ann. Phys. (Paris) 10, 908 (1955).

[31] R. Loudon, Advan. Phys. 13, 423 (1964); 14, 621 (1965).

[32] C. H. Henry, J. J. Hopfield, and L. C. Luther, Phys. Rev. Letters 17, 1178 (1966).

[33] D. D. Manchon, Jr., and P. J. Dean, in *Proceedings of the Tenth International Conference on the Physics of Semiconductors, Cambridge, Massachusetts*, edited by S. P. Keller, J. C. Hensel, and F. Stern (USAEC Division of Technical Information Extension, Oak Ridge, Tenn., 1970), p. 760. This paper gives references to much earlier work.

[34] W. Kohn, in *Solid State Physics*, edited by F. Seitz and D. Turnbull (Academic, New York, 1957), Vol. 5, p. 257.

[35] G. B. Wright and A. Mooradian, Phys. Rev. Letters 18, 608 (1967).

[36] W. Kohn and J. M. Luttinger, Phys. Rev. 98, 915 (1955).

[37] A. Baldereschi and M. G. Diaz, Nuovo Cimento 68B, 217 (1970).

[38] W. M. Saslow and D. L. Mills, Phys. Rev. 187, 1025 (1969).

[39] B. B. Varga, Phys. Rev. 137, A1896 (1965).

[40] K. S. Singwi and M. P. Tosi, Phys. Rev. 147, 658 (1966).

[41] R. E. Slusher and C. K. N. Patel, Phys. Rev. 167, 413 (1968).

[42] F. A. Blum and A. Mooradian, in Ref. 33, p. 755.

[43] J. F. Scott, T. C. Damen, J. Ruvalds, and A. Zawadowski, Phys. Rev. B 3, 1295 (1971).

[44] A. Mooradian and A. L. McWhorter, in *Light Scattering Spectra of Solids*, edited by G. B. Wright (Springer-Verlag, New York, 1969), p. 297.

[45] P. J. Colwell, Ph. D. dissertation (University of Illinois, Urbana, 1971) (unpublished).

[46] R. L. Hartman and P. J. Dean, Phys. Rev. B 2, 951 (1970).

[47] W. J. Choyke, D. R. Hamilton, and L. Patrick, Phys. Rev. 133, A1163 (1964).

[48] L. Patrick, Phys. Rev. 138, A1477 (1965).

[49] L. Patrick, Phys. Rev. B 5, 2198 (1972).

[50] U. Fano, Phys. Rev. 124, 1866 (1961).

[51] U. Fano and J. W. Cooper, Phys. Rev. 137, A1364 (1965).

[52] D. L. Rousseau and S. P. S. Porto, Phys. Rev. Letters 20, 1354 (1968).

[53] J. F. Scott, Phys. Rev. Letters 24, 1107 (1970).

[54] R. S. Katiyar, J. F. Ryan, and J. F. Scott, Phys. Rev. B 4, 2635 (1971).

[55] P. J. Colwell, W. D. Compton, M. V. Klein, and L. B. Schein, in Ref. 33, p. 484.

[56] L. Patrick, D. R. Hamilton, and W. J. Choyke, Phys. Rev. 132, 2023 (1963).

[57] D. C. Hamilton and A. L. McWhorter, in Ref. 44, p. 309.

[58] P. A. Wolff, Phys. Rev. 171, 436 (1968).

[59] M. V. Klein, B. N. Ganguly, and P. J. Colwell, Phys. Rev. B (to be published).